Visual processing in V1 is optimized on the edge of criticality

M. Girardi-Schappo,[1] G. S. Bortolotto,[1] J. J. Gonsalves,[1]
L. T. Pinto,[2] and M. H. R. Tragtenberg[1,*]

[1] *Departamento de Física, Universidade Federal de Santa Catarina, 88040-900, Florianópolis, Santa Catarina, Brazil*

[2] *Departamento de Engenharia Química e de Alimentos, Universidade Federal de Santa Catarina, 88040-900, Florianópolis, Santa Catarina, Brazil*

(Dated: October 1, 2015)

Abstract

Activity in the brain propagates as waves of firing neurons, namely avalanches. These waves' size and duration distributions have been experimentally shown to display a stable power-law profile, long-range correlations and $1/f^b$ power spectrum *in vivo* and *in vitro*. We study an avalanching biologically motivated model of the Macaque monkey primary visual cortex and find a minimum of the processing information time as function of the excitatory postsynaptic potential parameter (EPSP). Surprisingly, this point lies on the edge of a critical phase transition where avalanches are power-law distributed and have a $1/f^b$ power spectrum, matching experiments. The phase transition point is analytically determined by a mean field calculation and is close to the expected experimental value of EPSP in the cortex.

PACS numbers: 05.70.Jk,45.70.Ht,87.19.lt

* marcelotragtenberg@gmail.com

I. INTRODUCTION

The most important feature of a living complex system to survive is adaptability. In order to adapt, the organism cannot be inflexible, but also cannot act randomly. The border of chaos or a critical behavior seems to be the best evolutionary choice to survival beings [1]. Turing conjectured a similar idea referring to our minds and learning machines [2].

More recently, brain criticality have become a trendy research subject [3–5]. Some believe that the brain became critical by self-organization and selection [3], analogously to the sand-pile self-organized criticality (SOC) [6]. Criticality have the advantages of maximizing the response dynamic range [7] of neural networks, optimizing memory and learning processes [8], the computational power of the brain [9] and information processing flexibility [10].

The brain critical state is characterized using standard equilibrium statistical mechanics tools, as usual for non-equilibrium phase transitions [11]. The main features of the critical brain are scale invariance [11, 12], long-range spatial and temporal correlations [11, 13, 14], power-law (PL) avalanche distributions and $1/f^b$ power spectrum [15]. All of them have been experimentally found in neural networks either *in vitro* or *in vivo* [16–25]. However PL alone has been questioned as insufficient evidence for the critical regime [9, 26]. We argue that a sufficient criterion is the finite-size scaling (FSS) of a continuously varying order parameter [11] additionally to the PL distributed avalanche sizes and duration [15], which may follow Sethna's relation [27].

Here we show that the visual processing is optimized near a critical phase transition. Interestingly, it happens inside a Griffiths phase in which the density of activated neurons, the largest avalanche and the avalanche size distributions are scale invariants – these features are observed experimentally [19, 21, 22, 25]. Throughout the critical region, the power spectrum is of the form $1/f^b$, with $0.18 \leq b \leq 1.7$ as experimentally expected [16–18, 20, 24].

The control parameter is the *excitatory postsynaptic potential* (EPSP) and the critical region is found close to the experimental values of EPSP in the cortex [28–30]. The EPSP threshold for a complete network activation is approximated via a mean-field calculation and is also close to the numerical and experimental values of the parameter. Such control parameter allow for experimental validation of the model.

The avalanches spontaneously emerge during the constant stimulation of the retina, instead of artificially imposing a Poisson stimulus as in most of the brain critical models

(see [7, 8, 21, 25, 31–34] to cite a few). Scale-free avalanche dynamics is thus essential for the reliable processing of information in our model.

II. MODEL

The model for the primary visual cortex (V1) of the macaque monkey consists of interconnected square layers (linear size L) propagating the signal directionally from the retina towards secondary visual cortex (V2) [35]. Only four layers from the form recognition pathway within V1 are selected: the lateral geniculate nucleus (LGN) and the layers II/III, IVCβ and VI. The LGN layer consists of only its parvocellular neurons, which synapses are mostly connected to V1 layer IVCβ [36–39]. Synaptic buttons density is also based on experiments [36–39]. The network has $N = 4L^2$ neurons and forms square columnar structures, each with $N_c \approx 200$ neurons. Further details on the network architecture are discussed in Methods.

Each neuron i is composed of a compartmental dendrite [$d_m^{(i)}(t);\ m = 1, \cdots, 100$, Eq. (1)], the soma [$v_i(t)$, Eq. (2)], and a compartmental axon [$a_k^{(i)}(t);\ k = 1, \cdots, 10$, Eq. (3)]. The action potential advances one compartment per time step t, coming from the dendrites through the soma to the last axonal compartment:

$$\begin{aligned} d_1^{(i)}(t+1) &= \lambda E \sum_{j,n} a_n^{(j)}(t) \ , \\ d_k^{(i)}(t+1) &= \lambda \left[d_{k-1}^{(i)}(t) + E \sum_{j,n} a_n^{(j)}(t) \right], \text{for} k > 1, \end{aligned} \tag{1}$$

$$v_i(t+1) = \begin{cases} \Theta\left(d_{100}^{(i)}(t) - v_T\right) & , \text{if } v_i(t) = 0 \ , \\ -R & , \text{if } v_i(t) = 1 \ , \\ v_i(t) + 1 & , \text{if } v_i(t) < 0 \ , \end{cases} \tag{2}$$

$$\begin{aligned} a_1^{(i)}(t+1) &= \Theta\left(v_i(t)\right) \ , \\ a_k^{(i)}(t+1) &= a_{k-1}^{(i)}(t), \text{for } k > 1, \end{aligned} \tag{3}$$

where $\lambda = 0.996$ is the attenuation constant (chosen to match experimental attenuation [28]), $v_T = 10$ mV is the firing threshold, R is the refractory period and $E > 0$ is the EPSP (which has values of the order of 1 mV [28–30]). R is adjusted equal to total simulation time to reproduce adaptation in the visual system [40] and to allow us to define network processing time. The double sum in Eq. (1) is over all the axonal compartments of presynaptic neuron j

connected to the dendritic compartment of the postsynaptic neuron. The different quantities of compartments for dendrites and axons in a single neuron model the different velocities of the signal propagating in them [41].

Initial conditions are $a_k^{(i)}(0) = d_m^{(i)}(0) = v_i(0) = 0 \ \forall \ (k, m, i)$. A 30×30 square of photoreceptors near the corner of the Input layer is constantly active in order to start activity. Then, interspersing small and large avalanches spontaneously emerge due to the propagation of action potentials through dendrites and axons. We do not impose over the system the separation of timescales, as commonly done in SOC models [15]. The only LGN neurons that fire are the ones receiving input from the retina, so the order parameters will saturate close but not equal to unity in the following results. Results are stable to different initial conditions.

III. RESULTS AND DISCUSSION

The activity of the network is the sum of all the neurons firings at each time step and the system's *processing time* is the instant of the last spike of the network, marked with arrows in Fig. 1A. We define the size s of an *avalanche* as the sum of all the activity between two consecutive instants of silence, similarly to the experimental procedure [21]. In fact, each s is the area under each of the peaks in Fig. 1A.

We analyze the phase transition by defining two order parameters: the density ρ of activated neurons [43, 44] and the fractional size $m \equiv M/N$ of the largest avalanche [43, 44] (M is the size of the largest avalanche). Notice that the Blume-Emery-Griffiths model also exhibits two order parameters [45]. Near the critical point, we may write [11, 12, 43, 44]:

$$\rho(E; L) = L^{-\beta/\nu_\perp} \bar{\rho}(|E - E_c| L^{1/\nu_\perp}) \ , \tag{4}$$

$$m(E; L) = L^{-D} \bar{m}(|E - E_c| L^{1/\nu}) \ , \tag{5}$$

$$\chi_\rho(E; L) = L^{\gamma/\nu_\perp} \bar{\chi}_\rho(|E - E_c| L^{1/\nu_\perp}) \ , \tag{6}$$

where β, $\nu_\perp$, D, ν and γ are scaling exponents and $\bar{m}(x)$, $\bar{\rho}(x)$ and $\bar{\chi}_\rho$ are universal scaling functions. $\chi_\rho \equiv N \left(\langle \rho^2 \rangle - \langle \rho \rangle^2 \right) / \langle \rho \rangle$ is the susceptibility related to the order parameter ρ [42]. The phase transition occur on E_c.

We also measure the avalanche size distributions, $\mathcal{P}(s)$, and complementary cumulative distributions, $\mathcal{F}(s)$, the network processing time, T, and the avalanches' autocorrelation,

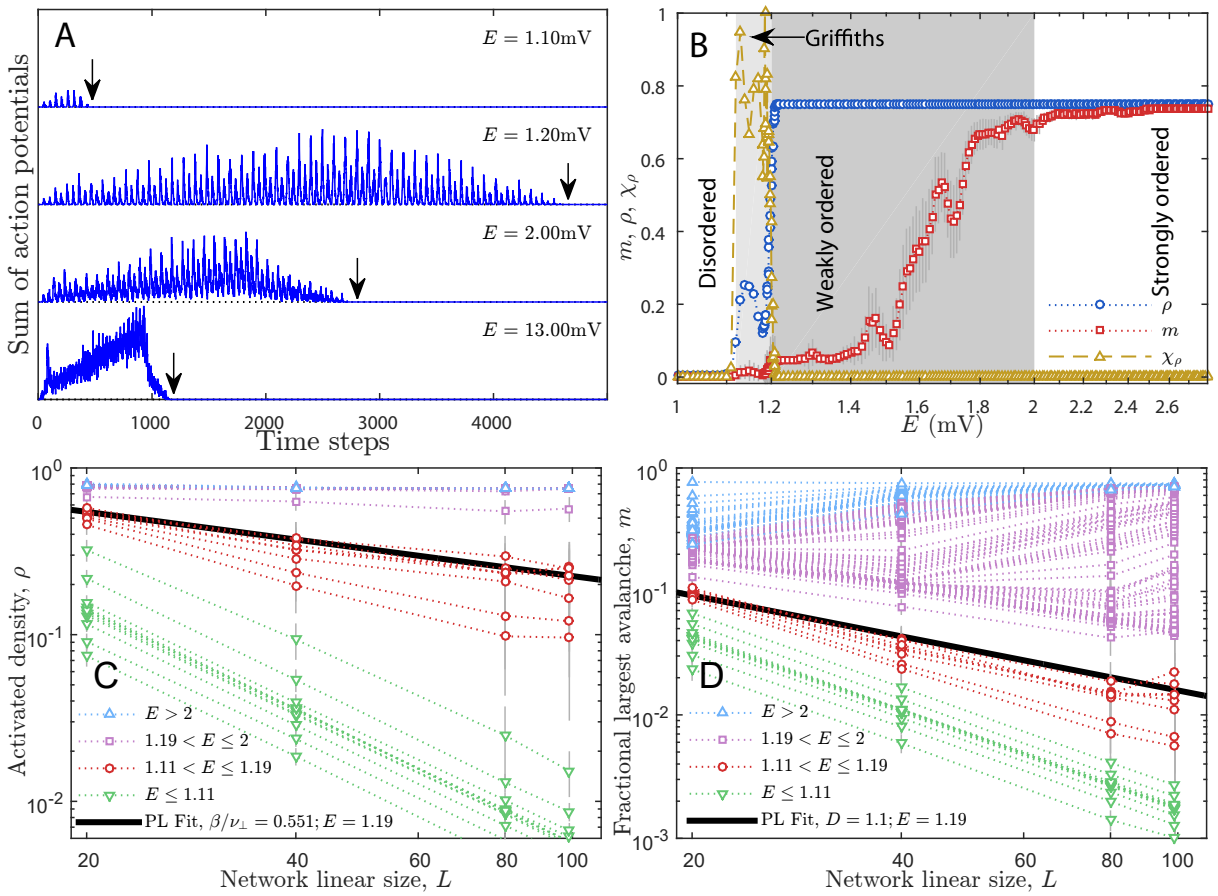

FIG. 1. Network activity and order parameters. Panel A: Temporal profile of the avalanches for many EPSP. Arrows mark the processing time T of the network. For $E = 1.1$ mV, only very small avalanches occur; $E = 1.2$ mV shows many small avalanches; for $E = 2.0$ mV there is a dominating avalanche (compare to the dotted line that marks zero activity); and for $E = 13.0$ mV the dominating avalanche takes over all the dynamics. Panel B: Density of activated neurons ρ during total activity time, fractional largest avalanche m and $\chi_\rho = N\left(\langle\rho^2\rangle - \langle\rho\rangle^2\right)/\langle\rho\rangle$ [42] as function of E for $L = 99$. χ_ρ is normalized to unity for visualization. Panel C: FSS of ρ order parameter [43, 44] yielding scaling exponent $\beta/\nu_\perp = 0.55(3)$ – Eq. (4). Panel D: FSS of m order parameter [43, 44] yielding scaling exponent $D = 1.1(1)$ – Eq. (4). Both fits were on the transition point $E_c = 1.19$ mV . D may be fitted for every E in order to be compared with the largest avalanche collapse exponent, D' (see text). Vertical bars are standard deviation, light gray indicates Griffiths phase and dark gray, weakly ordered phase.

$C(t')$, and power spectrum, $S(f)$ (the latter may be compared with experimental data [16,

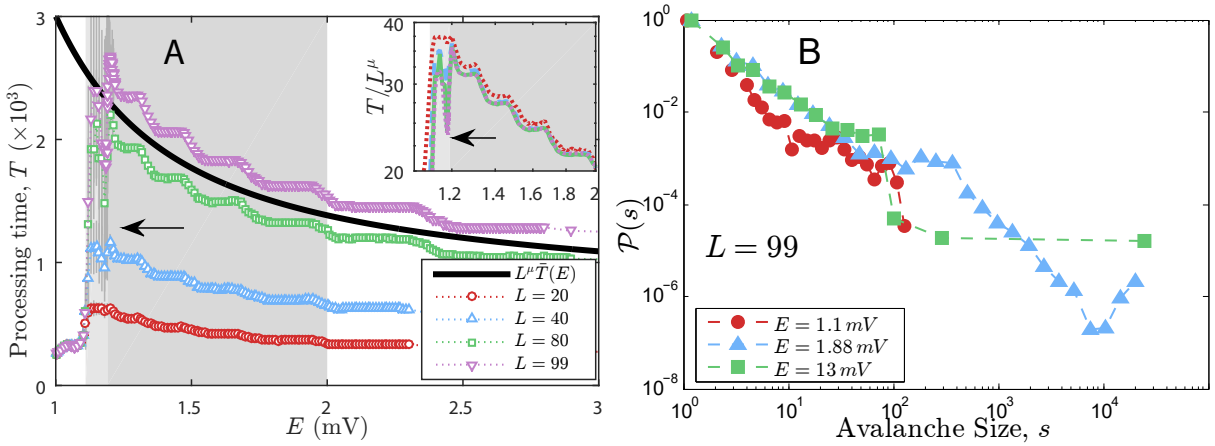

FIG. 2. Processing time and avalanche size distributions. Panel A: Processing time T as function of E for many L. Solid line indicates the asymptotic behavior of T given by $L^\mu\bar{T}(E)$. Panel A inset: collapse plot $\bar{T} = T/L^\mu$ with $\mu = 1.0(1)$. Arrows indicate the minimum of T, vertical bars are standard deviation (notice they are maximal in the light gray region), light gray is the Griffiths phase and dark gray is the weakly ordered phase. Panel B: avalanches sizes distributions $\mathcal{P}(s)$ for $L = 99$ and three different E. Note the bump around avalanches of size 200 for $E = 1.88$ mV. This bump reveals the internal structure of the network. See text for discussion.

20, 24]):

$$\mathcal{F}(s) \sim s^{1-\alpha}\mathcal{G}\left(s/M\right) \ , \tag{7}$$

$$T\left(E;L\right) = L^{\mu}\bar{T}\left(E\right) \ , \tag{8}$$

$$C(t') \sim t'^{-\theta}\exp\left(-t'/\tau\right) \ , \tag{9}$$

$$S(f) \sim f^{-b} \ , \tag{10}$$

where α is the exponent of avalanche sizes distribution, $M \sim L^{D'}$ is the largest avalanche, μ is a scaling exponent, $\bar{T}(E)$ is a universal scaling function, t' is the time lag between two avalanches, τ is the characteristic time of the autocorrelation cutoff and θ and b are the autocorrelation and power spectrum exponents, respectively. As $S(f)$ is the Fourier transform of $C(t')$, $\theta + b = 1$ for $C(t')$ in the power-law regime. Also, notice that $D' = 2 - D$ because $M \sim 4mL^2$.

In typical critical systems, $\tau \sim L^z$ defines the dynamical exponent, z [11, 13, 43, 44]. However, in Griffiths phases, $\tau \sim \exp\left(cL^{D'}\right)$, where D' defines a typical dimensionality of the system and is the scaling exponent of the largest avalanche [43, 44]. Additionally, χ_ρ is expected to be maximized during the whole extended critical region.

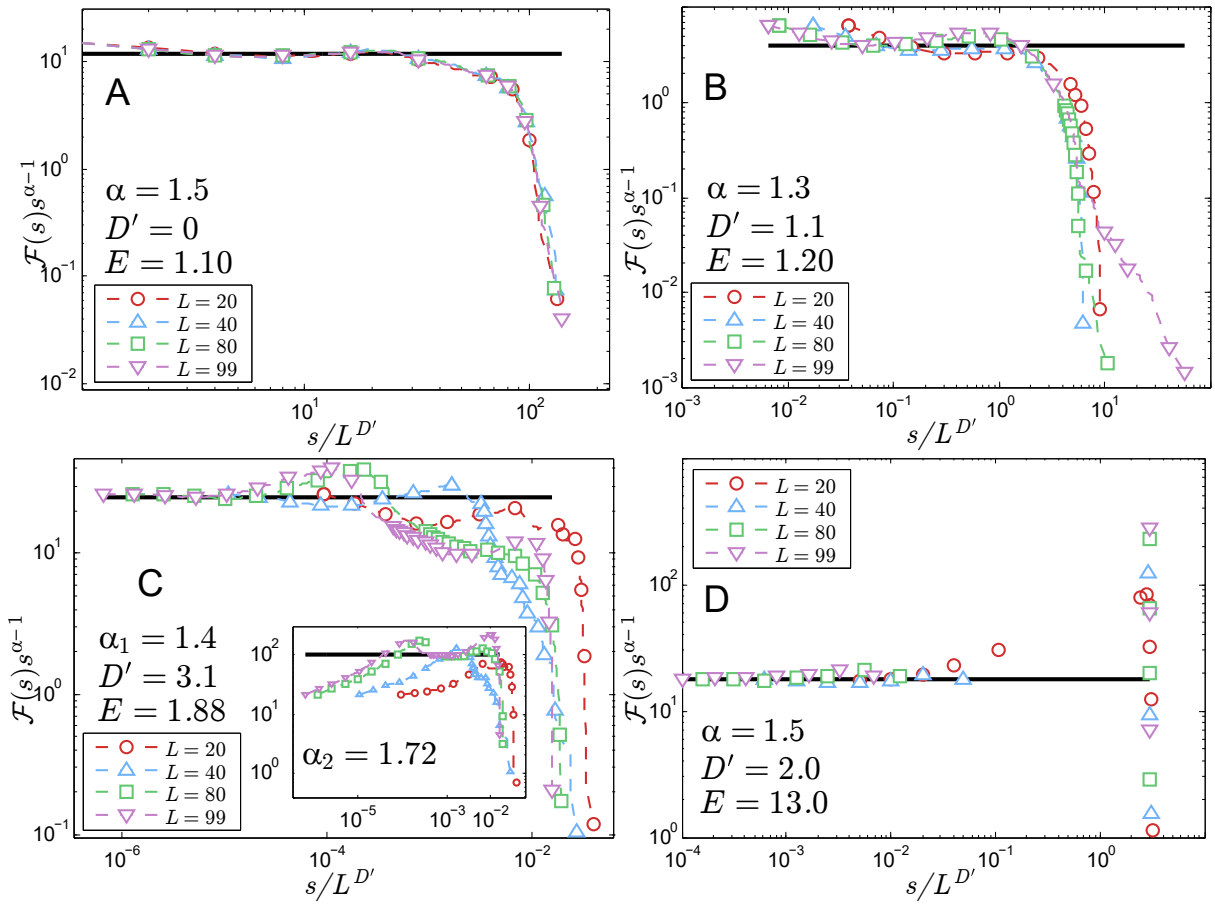

FIG. 3. Avalanche sizes cumulative distributions. Panel A: Cumulative distribution collapse of avalanches in disordered phase. Avalanches do not scale with system size ($D' = 0$) but present a PL regime with exponent $\alpha = 1.5(1)$. The PL region is due to noisy activity in the LGN since only small and very short avalanches are present. Panel B: Cumulative distribution collapse of avalanches in Griffiths phase with exponents $\alpha = 1.3(1)$ and $D' = 1.1(1)$. Panel C: Cumulative distribution collapse of avalanches in weakly ordered phase with exponents $\alpha_1 = 1.4(1)$, $\alpha_2 = 1.72(8)$ and $D' = 3.1(3)$. The bump separating both PL regimes is a consequence of the columnar structure of the network, as it lies where $s \approx N_c$. Panel D: Cumulative distribution collapse of avalanches in strong ordered phase with exponents $\alpha = 1.5(1)$ and $D' = 2$. The gap in this distribution shows that processing occurs rather through a large dominating avalanche, so the PL scaling represents only noisy avalanche activity in the LGN. The straight black lines guide the eyes over the collapse of the PLs. Notice that α is the exponent of $\mathcal{P}(s)$ as well. $D' = 2 - D$ is approximately obeyed.

Activity spreads as spiking circular waves throughout the layers as well as inside them. In this work, we focus on the temporal profile of the activity, shown in Fig. 1A.

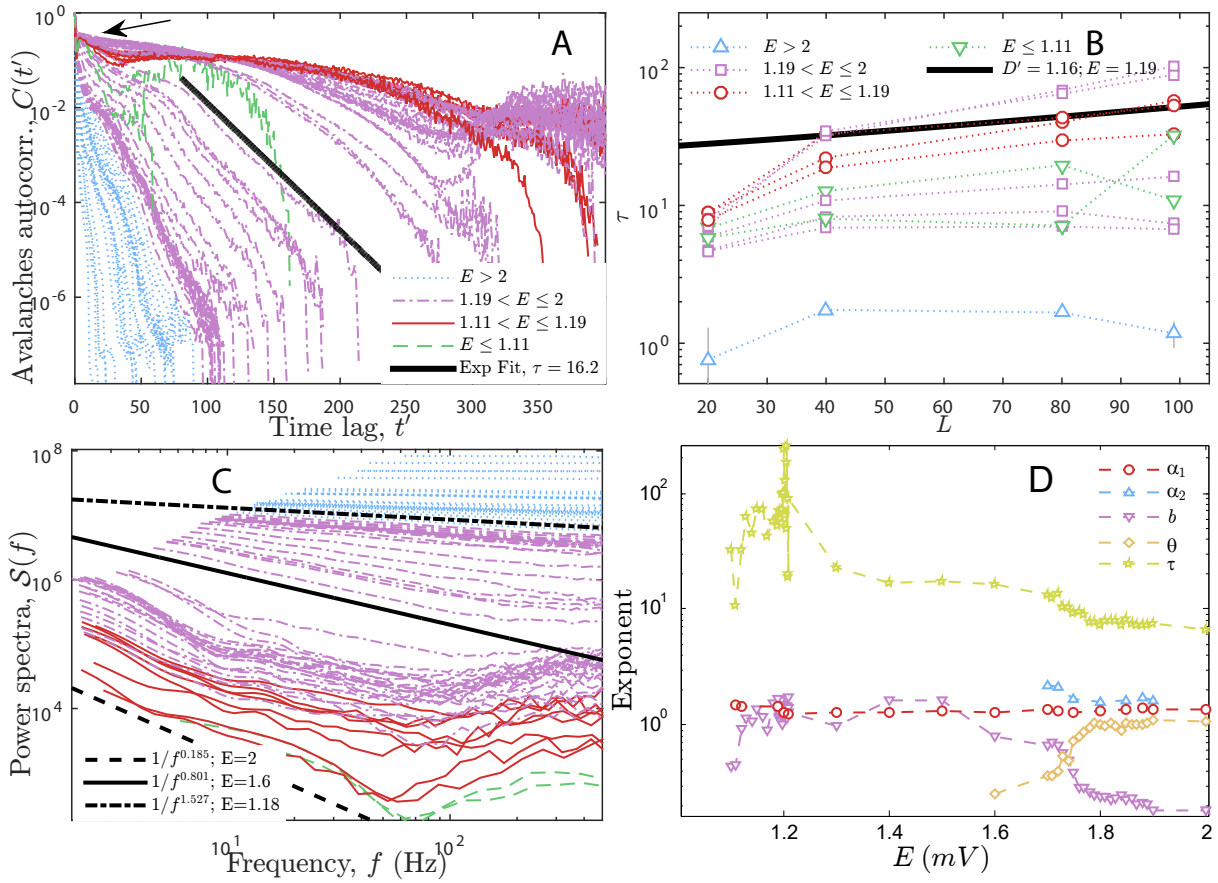

FIG. 4. Autocorrelation, power spectrum and exponents overview. Panel A: Average autocorrelation of avalanche sizes time series for $L = 99$ and many E. The solid line shows the exponential fit to the autocorrelation cutoff for $E = 1.6$ mV giving $\tau = 16.2$ time steps. The arrow indicates the region in which $C(t') \sim t'^{-\theta}$. Panel B: Scaling law $\tau(L)$ for many E. Ignoring $L = 20$, $\tau \sim \exp\left(L^{D'}\right)$ for $1.12 \leq E \lesssim 1.2$ mV characterizing the Griffiths phase [43, 44]. Panel C: Average power spectra of avalanche sizes time series for $L = 99$ and many E. The straight lines indicate the fit $S(f) \sim f^{-b}$ for $E = 1.18$ mV, 1.6 mV and 2 mV as examples. Notice how the curves' slope smoothly vary and yield $b \gtrsim 1$ inside the Griffiths phase (see panel D too). Color code corresponds to that of panels A and B. Panel D: Overview of how exponents vary according to E. α_1 and α_2 (only present in the weakly ordered phase) are the avalanche size distribution exponents, b is the power spectrum exponent, θ is the autocorrelation exponent and τ is the autocorrelation characteristic time. μ, ω and $\beta/\nu_\perp$ are not shown because they do not change. D is zero in the disordered phase and does not change for $E < E_c$. Exponent θ is negative for $E < 1.6$ mV so it does not appear in the logarithmic y-axis.

A. Mean-field approximation

It is clear in Fig. 1A that there is a change in the activity profile as E is varied. The signal may reach only a few neurons of each layer for $E = 1.1$ mV whereas for $E > 1.19$ mV, it excites the whole network. Such a behavior arises from the competition between excitation and dissipation.

At the point where excitation balances dissipation, one expects that every neuron in the network will fire once. We will call this point the *activation threshold*, where $E = E_{th}$. In order for any neuron i to fire, the signal that reaches the soma should be greater than or equal to the firing threshold, v_T:

$$n_{in}^{(i)} \left\langle d_{100}^{(i)} \right\rangle \geq v_T \quad , \tag{11}$$

where $n_{in}^{(i)}$ is the average amount of inward synapses per dendritic compartment of the post-synaptic neuron i, $\left\langle d_{100}^{(i)} \right\rangle = r_{100}^{(i)}(\lambda)E$ is the average signal arriving on the soma compartment from one single synapse on any dendritic compartment of neuron i and $r_{100}^{(i)}(\lambda) = \lambda^{50(1+\ln\lambda)}$ is the fraction of the signal that reaches the soma as function of λ from a single presynaptic cell. See Methods for a derivation of $\left\langle d_{100}^{(i)} \right\rangle$.

As the structure of the network is fixed, we may estimate $n_{in}^{(i)} \approx 6.244$ [see Table (II)]. It is then simple to calculate E_{th} from Eq. (11): $E_{th} = v_T / \left[n_{in}^{(i)} r_{100}^{(i)}(\lambda) \right] \approx 1.95$ mV, which is close to the average experimental value of the E in the cortex [28–30].

It is important to notice how simplistic this approximation is: $\left\langle d_{100}^{(i)} \right\rangle$ will depend on the distribution of $n_{in}^{(i)}$ over the dendritic compartments, which in turn depends on the quantity of dendritic compartments. The more synapses arriving per dendritic compartment the smaller E_{th} will be. For instance, if we use the values of Table I, then $n_{in}^{(i)} = 6.5$ and $E_{th} \approx 1.88$ mV.

B. Computational results

We performed between one hundred and three hundred realizations of the system for each EPSP of each L in order to calculate averages [Eqs. (4) to (10)] and standard deviations (vertical bars in Figs. 1 and 2).

Fig. 2A shows that the processing time has a non-monotonic behavior (clearer in the inset), with a sharp rise, followed by a deep minimum at $E = 1.18$ mV (pointed by arrow)

and another sharp rise, reaching its highest value at $E = 1.21$ mV. After that, T slowly decays asymptotically towards a constant through a landscape full of shallow minima. The asymptotic behavior of $T(E; L)$ for $E > E_c = 1.19$ mV (the solid black curve in Fig. 2A) is a crossover of two power laws (PL),

$$\bar{T}(E) \sim \left(E^{-\omega} + E^{-1/\omega}\right) \ , \tag{12}$$

where $\omega = 3.1(2)$. The scaling exponent of the processing time is $\mu = 1.14(6)$, as described by Eq. (8).

Fig. 1B shows the density of activated neurons during whole simulation time, the fractional largest avalanche and the ρ susceptibility as functions of E for $L = 99$. χ_ρ is maximum in the range $0.12 \lesssim E \lesssim 1.2$ and has a sharp peak at $E \equiv E_c = 1.196$ mV. We conclude that this range corresponds to a Griffiths phase, which we check further on via the scaling analysis of the autocorrelation characteristic time. Note that E_c is even closer to experimental values of EPSP in the cortex [28–30]).

The FSS analysis of ρ in Fig. 1C shows that the phase transition occurs at $E_c = 1.19(1)$ mV (which is of the same order as our naive mean-field calculation) with scaling exponent $\beta/\nu_\perp = 0.55(3)$ [Eq. (4)]. The deep minimum in T lies then on the onset of the phase transition. Additionally, T has maximum standard deviation during all the Griffiths region, meaning that although the system process information quickly in average, it is flexible enough to adapt to external input as suggested by experimental work [25]. Therefore the processing of information may reliably occur only around this region. The FSS of χ_ρ, not shown, yields $\gamma/\nu_\perp = 3.1(2)$ [Eq. (6)].

The FSS analysis of m in Fig. 1D shows that a dominating avalanche appears slowly as E increases (both in size and duration, the latter pictured in Fig. 1A) starting from E_c with scaling exponent $D = 1.1(1)$ [Eq. (5)]. Both order parameters mark a dynamical *order-disorder* continuous phase transition because the structure of the network is always disordered (see Methods).

Fig. 2B shows the distribution of avalanche sizes s for $L = 99$ and three typical EPSP. The three distributions have PL dependence $\mathcal{P}(s) \sim s^{-\alpha_1}$ on small s. These avalanches happen mainly during the passage of the signal through the LGN layer, when activity is starting to propagate in the network. For $E = 1.1$ mV no larger avalanche appears whereas for $E = 13$ mV there is only one single large avalanche. However, in between these two

regimes there is a region in which many large avalanches slowly appear as E is increased (the weakly ordered regime of Fig. 1B). The large avalanches in this regime are also PL distributed with exponent α_2.

Figs. 3A–D show the collapse plot of the complementary cumulative distributions of the avalanche sizes, $\mathcal{G}(s/M) \sim \mathcal{F}(s)s^{\alpha-1}$ with $M \sim L^{D'}$ from Eq. (7), used to estimate α and the cutoff exponent of the largest avalanche, D'. We found values $1.3 \leq \alpha_1 \leq 1.5$ and $\alpha_2 \approx 1.7$. These values agree very well with experiments [19, 25] and with Maximum Likelihood estimation (see Methods).

Sethna's relation [27] [$a = (\tau - 1)/(\alpha - 1)$, where τ is the exponent of avalanche duration distribution] is sometimes used to determine the system's critical point [25]. This relation holds for all distributions shown in Figs. 2B and 3 within less than 10% error, whether in the disordered, Griffiths or ordered phases. Therefore care should be taken when using solely this relation to check for criticality, as also noted by other authors [26].

The largest avalanche scales according to $D' = 0$ in the disordered phase, as expected. In the ordered phase, $D' = 2$ meaning that the avalanches are spreading simultaneously inside each layer. The Griffiths phase (including the transition point) has $D' = 1.1(1)$. The surprising scaling of avalanche distributions in the critical region means that avalanches are spreading mainly inside V1 model columns via a branching process (the signal goes back and forth through the feedback loop between layers VI and IVCβ). Notice that these values follow the expected relation $D' = 2 - D$ (having D' and D independently estimated).

The bump around avalanches of size $s \approx 200 \approx N_c$ is a characteristic scale for small avalanches in the weakly ordered regime because it does not scale with system size. It is then caused by the amount of neurons in the columns of our V1 model. If the number of neurons in a column N_c tended to N this bump would vanish, leaving the system with only one characteristic scale and one exponent α similarly to the model presented by Teramae & Fukai [46].

We also determine the scaling of the avalanche time series autocorrelation characteristic time, τ, which is expected to be exponential inside the Griffiths phase [43, 44]. Fig. 4A shows $C(t')$ for many E and $L = 99$. Each curve has been averaged over several trials. We assume $C(t')$ to follow Eq. (9) and fit its exponential cutoff for each E and L to obtain τ (e.g. the solid black curve in Fig. 4A).

The scaling law $\tau(L)$ is plotted in Fig. 4B. We show the fit of $\tau \sim \exp\left(cL^{D'}\right)$ for $E =$

1.19 mV ignoring $L = 20$ (the thick solid black line) yielding $D' = 1.1(1)$ inside the Griffiths region. This result agrees with our expectation that D' should be the scaling exponent of the largest avalanche [43, 44]. However, our data may also be fitted by $\tau \sim L^z$ yielding $z = 1.0(1)$ (not shown) if $L = 20$ is considered. Therefore, we rely mostly on the fact that the susceptibility χ_ρ diverges inside the range $1.12 \leq E \lesssim 1.2$ mV to conclude that it is indeed a Griffiths phase [47].

We have ignored $L = 20$ points for fitting in Fig. 4B because each of the $L = 20$ network's columns includes a fraction of more than 12% of all its neurons, which is significantly different from the other L network column fractions (3% for $L = 40$ and less than 1% for $L = 80, 90$). Avalanches thus are able to grow larger and faster than expected in $L = 20$ networks than for other L with fixed E.

The power spectrum shows a stable f^{-b} behavior with $b \gtrsim 1$ inside the Griffiths phase (see Fig. 4C). In general, b varies in the interval $[0; 1.7]$ agreeing very well with experimental results for the visual cortex [16, 20, 24]. Fig. 4 summarizes how all the exponents of our study vary with E. Exponent θ for $E < 1.6$ mV do not appear in the figure because it is negative. α_2 only appears inside the weakly ordered phase where the second scale is noticeable.

IV. CONCLUDING REMARKS

We studied a model for the primary visual cortex presenting its characteristic columnar structure. The key elements of this model are the neurons dynamical structure and dendritic excitation/dissipation balance. While the delay due to action potential propagation in the dendrites and axons causes the avalanches, the signal attenuation balances the network information processing. If we were to model lateral inhibition inside the layers, we would expect the activation threshold to grow leaving the dynamics generally unaltered.

We verified that the network processing time quickly decays as E reaches the critical point. The network activation threshold and the phase transition point are close to the average value of EPSP in the cortex [28–30]. The network is able to reliably process information only within a limited E range around the Griffiths and weakly ordered phases because only in this region the variability of the response is maximal and the processing time is minimum allowing for adaptation in the system's response. In the other phases either the network will

respond with noisy activity or will fire a single dominating avalanche.

The model columnar structure was evidenced in the characteristic scale of small avalanches in the avalanches sizes distributions in the weakly ordered regime. We hypothesize then that the two power-law regimes could be experimentally found if one were able to directly measure spike avalanches in V1 (not simply local field potentials), because V1 is naturally organized in columns [48].

The Griffiths phase presence is confirmed by the divergence in the susceptibility, although the scaling law of the autocorrelation cutoff characteristic time is inconclusive. Inside it, the model exhibits $1/f^b$ power spectrum with $b \gtrsim 1$ which accurately matches experimental results [16, 18, 20, 24]. Our study stresses that being quasi-critical is advantageous for the brain sensory networks and could be further used to help the development of pattern recognition applications because of the short processing time near the critical point.

We conjecture that the studied model belongs to Dynamical Percolation-like universality class because its dynamics resembles that of the generalized epidemic process with immunization [11, 49]. The network structure was shown to fundamentally shape the dynamics of the system, so we are working to define a measure of its dimensionality in order to be able to better characterize its universality class.

Some future work may focus on improving some of the model's features, like: the excitatory field of each neuron may change with depth; disorder in E; synaptic dynamics or plasticity [25, 31, 32] to model adaptability; and lateral inhibition. Finally, we hope to provide here a kinematic framework for microscopic cortical modeling.

V. ACKNOWLEDGMENTS

We thank J-P Thivierge for providing the code for Maximum Likelihood test and S. Boettcher for discussions.

VI. METHODS

A. Network architecture

The full network has $N_{full} = 2N_{io} + N$ elements, where $N = 4L^2$ is the amount of neurons composing the internal layers (LGN, VI, IVCβ and II/III, each with L^2 neurons),

$N_{io} = (10L)^2$ is the amount of elements in each of the input/output layers. An example of the look of the network is in Fig. 5A for $L = 5$. The architecture of the network is illustrated in Fig. 5B, where arrows point the direction of the connections towards which the signal is propagated.

Layers are stacked as shown in Figs. 5B,C. We can assign each element i with a spatial position, $\vec{r_i} = (x_i, y_i, z_i)$, labeling layers from Input ($z_i = 0$) to Output ($z_i = 5$) and integers $(x_i, y_i) \in [1; L] \times [1; L]$. The elements of the input layer are the photoreceptors of the retina. The elements of the output layer are only the axonal terminals which would connect to dendrites in the secondary area of the visual cortex (V2). The elements of the remaining internal layers are neurons.

There is a matrix of 10×10 photoreceptors positioned in front of each neuron of the LGN (i.e. N_{io} photoreceptors). On the other end of the network, each neuron in layer II/III sends 100 synapses towards V2 (i.e. a total of N_{io} axonal terminals would connect to V2). The 100 axonal terminals of a given neuron are positioned in front of it, randomly distributed inside a 10×10 matrix.

All the connections are chosen and fixed in the beginning of the simulation (quenched disorder). The amount of connections that each element of a given layer attempts to send to any adjacent layer is in Table (I). Boundary conditions are free, which means that any attempted synapse that would fall outside of the ranges of the postsynaptic layer are discarded. Thus, the actual number of synapses per presynaptic element is a little smaller than the values in that table.

Table (II) shows the amount of synapses that a given element of any layer receives. The network is symmetric in average in the sense that mean number of synapses per presynaptic neuron is almost equal to the mean number of synapses per postsynaptic neuron. Tables (I) and (II) also show the adjacency of layers.

In order to create a connection, each presynaptic neuron, j, projects its axon towards a region of $l^2 = 7 \times 7$ neurons of an adjacent layer. The postsynaptic neurons in this region are then randomly selected via a bidimensional Gaussian distribution, $\mathcal{P}_G(x, y; x_j, y_j, \sigma_d)$, centered in the (x_j, y_j) coordinates of the presynaptic neuron with standard deviation $\sigma_d = 3$ in each direction.

A columnar structure emerges in the network as a consequence of picking neighbors in the limited region of l^2 neurons. V1 experimentally displays such structure [48]. Therefore,

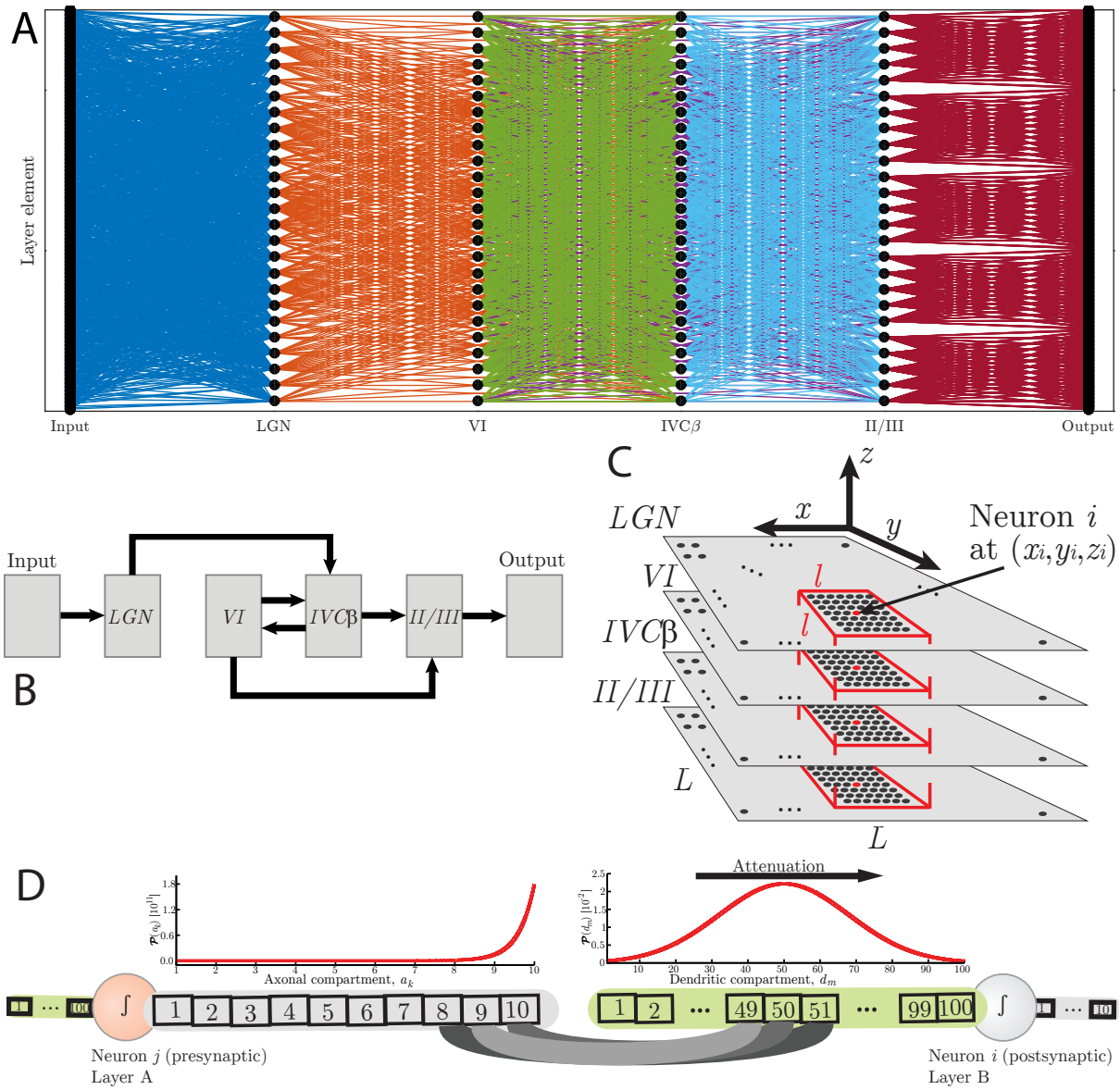

FIG. 5. Elements of the V1 model. A: A realization of the $L = 5$ network. Circles are photoreceptors (Input), neurons (internal layers) and axonal compartments (Output). Layers are linearized. B: Architecture of the network. C: Spatial organization of the network of $N = 4L^2$ neurons. The columnar structure is highlighted in red. There is a column of size $N_c = 4l^2 = 196$ neurons centered on each neuron of the network. D: Compartmental scheme of neurons. The probability, $\mathcal{P}(a_k)$, of choosing a presynaptic axonal compartment, a_k, of any neuron is exponential such that most of the synapses start from the end of the axon (left). The probability, $\mathcal{P}(d_m)$, of choosing a dendritic postsynaptic compartment, d_m, is Gaussian with mean 50 and standard deviation 10, so that most of the synapses lay in the middle of the dendrite (right).

From \ To	LGN	VI	IVCβ	II/III	Output
Input	1	-	-	-	-
LGN	-	-	500	-	-
VI	-	-	1100	350	-
IVCβ	-	600	-	700	-
II/III	-	-	-	-	100

TABLE I. The quantity of attempted synapses per presynaptic element from a specific layer (rows) to another layer (columns). Presynaptic element may be a photoreceptor (from Input layer) or a neuron (from internal layers). There are 100 photoreceptors in the Input layer for each neuron of the LGN. There are 100 axon compartments of each neuron in the II/III layer connecting to V2. These values are predefined in the beginning of the simulation, but are not exactly achieve in practice because of free boundary conditions.

each column has approximately $N_c = 4l^2 = 196$ neurons, see Fig. 5C. If one consider the loop between layers IVCβ and VI, then columns would virtually have $N_c = 5l^2 = 245$ neurons. The connections from Input layer to LGN are created using the same procedure.

Once pre and postsynaptic neurons are chosen, synapses are formed between one axonal compartment, $a_k^{(j)}$, chosen with exponential probability $\mathcal{P}_E(k) = (10/4)\exp(10k/4)$, of the presynaptic cell, j, and one dendritic compartment, $d_m^{(i)}$, chosen with Gaussian probability

From \ To	LGN	VI	IVCβ	II/III	Output
Input	98	-	-	-	-
LGN	-	-	488	-	-
VI	-	-	1073	293	-
IVCβ	-	585	-	683	-
II/III	-	-	-	-	1

TABLE II. The quantity of synapses per postsynaptic element that a specific layer (column) recieves from another layer (row). Postsynaptic elements are all neurons. There are 100 axonal compartments in the output layer for each neuron and each of them forms a synapse with V2. The averages were performed when assembling a $L = 99$ network and are similar to the values from Table (I).

$\mathcal{P}_G(m; d^{(c)}, \sigma_d)$, of the postsynaptic cell, i, where $d^{(c)} = 50$ and $\sigma_d = 10$. See Fig. 5D.

The probability of choosing a dendritic compartment is taken as Gaussian because consecutive events of connecting to any two compartments should be uncorrelated and most of the synapses should arrive around the center of the dendrites [28]. The probability of choosing an axonal compartment is exponential because axons should transport signals for as long as possible, thus most of the outward synapses must come from the end of the axon [36–39].

The neurons of this model could be mapped into simple celular automata, like the one studied by [7]. One should then adjust the probability of exciting a neighbor (in the referred model) as proportional to the fraction of the signal that would reach the soma in our model (derived in Appendix VI). Also, the amount of refractory states should be taken equal to the entire simulation time. Then, it is just a matter of building the structure of the network according to the rules presented in this section.

B. Macroscopic measurements

The *activity* of the network at time t, $A(t)$, is just the sum of all neurons firings at each time step,

$$A(t) = \sum_{i=1}^{N} \delta_{v_i(t),1} \ , \tag{13}$$

where $\delta_{i,j}$ is the Kronecker delta. The density of activated neurons (our first order parameter) is simply

$$\rho = \frac{1}{N} \sum_{t=0}^{T} A(t) \ , \tag{14}$$

where T is the processing time of the network (total simulation time). Notice that ρ thus defined is already normalized because each neuron may only fire once.

The avalanche size, $s(n)$, is the sum of network activity,

$$s(n+1) = \sum_{t=t_n}^{t_{n+1}} A(t) \ , \tag{15}$$

where $A(t_n) = 0 \ \forall \ n$. The largest avalanche is $M = \langle \max(s_n) \rangle$ (average is taken across several trials for each E) and the ratio $m = M/N$ – the fractional largest avalanche – is the second order parameter.

The avalanches autocorrelation function, $C(t')$, and power spectrum, $S(f)$, are defined as:

$$C(t') = \langle s(n)s(n-t')\rangle \ , \tag{16}$$

$$S(f) = \left| \int_{-\infty}^{+\infty} s(n) \exp\left(-2i\pi f n\right) dn \right|^2 \ . \tag{17}$$

The characteristic time, τ, of the correlation function is defined by the exponential cutoff fit of $C(t') \sim \exp\left(-t'/\tau\right)$ for large t'. Moreover, if $S(f) \sim f^{-b}$ and $C(t') \sim t'^{-\theta}$ for small t', then $b + \theta = 1$ because $S(f)$ is the Fourier Transform of $C(t')$.

C. Average signal in soma

Consider the structure described in Methods for the dendrites of the neurons and the dynamics described in the main text. If a single synapse arrives at the compartment $d_n(0)$ of some neuron in instant $t = 0$, then after $k-n$ time steps, the signal in dendrite $d_k(t = k-n)$ is $d_k = \lambda^{k-n}E$ with average $\langle d_k\rangle = \left\langle \lambda^{k-n}\right\rangle E$ (we omit time for simplicity).

The synapses arrive in any dendritic compartment, d_n, with Gaussian distribution $\mathcal{P}_G(n; 50, 10)$ with mean $d^{(c)} = 50$ and standard deviation $\sigma_d = 10$. Then, the average $\left\langle \lambda^{k-n}\right\rangle$ is given by:

$$\left\langle \lambda^{k-n}\right\rangle = \lambda^k \int_{-\infty}^{+\infty} \lambda^{-n} \mathcal{P}_G(n) dn \ , \tag{18}$$

where the integral is continuously evaluated within infinity limits because more than 99% of the Gaussian distribution lies within the bounds of the dendrite.

The integrand in Eq. 18 may be manipulated in order to still get a Gaussian function multiplied by a constant:

$$\left\langle \lambda^{k-n}\right\rangle = \lambda^{k-d^{(c)}+\sigma_d^2 \ln(\lambda)/2} \int_{-\infty}^{+\infty} \bar{\mathcal{P}}_G(n) dn \ , \tag{19}$$

$$\left\langle \lambda^{k-n}\right\rangle = \lambda^{k-d^{(c)}+\sigma_d^2 \ln(\lambda)/2} \tag{20}$$

where $\bar{\mathcal{P}}_G(n)$ is a normalized Gaussian with displaced mean. Notice that $r_k(\lambda) \equiv \left\langle \lambda^{k-n}\right\rangle = \langle d_k\rangle / E$ is the fraction of the signal that reaches compartment k.

If the synapse (or external signal) arrives localized at compartment $d^{(c)}$ (i.e. $\sigma_d = 0$), then $r_k(\lambda) = \lambda^{k-d^{(c)}}$ is a simple exponential decay with characteristic time $-1/\ln(\lambda)$, as experimentally expected [28]. Although in reproducing experiments, the arriving signal

compartment should be farther than 100 units from the soma. In our model, the signal that reaches the soma is the signal from $k = 100$. Thus, the average signal in soma is $\langle d_{100} \rangle = r_{100} E$.

D. Statistical Test

We performed a Maximum Likelihood test in our data. The columnar structure in the model is responsible for the presence of a *bump* in the format of avalanches distribution (see Fig. 3). To take this into account we used a censored Maximum Likelihood estimator which uses only the data that exhibits a power law. The formula follows the description for discrete power laws made by [50]:

$$\hat{\alpha} = \arg\max_{\alpha} [-n \ln \zeta\left(\alpha, s_{min}, s_{max}\right) + \mathcal{H}], \tag{21}$$

$$\mathcal{H} = \sum_{i=1}^{n} \begin{cases} \ln\left(\sum_{k=s_{min}}^{s_L} k^{-\alpha}\right) & \text{for } s_i = s_L \ , \\ \ln\left(\sum_{k=s_R}^{s_{max}} k^{-\alpha}\right) & \text{for } s_i = s_R \ , \\ \ln\left({s_i}^{-\alpha}\right) & \text{else} \end{cases} \tag{22}$$

where $s \geq s_{min} \geq 1$ and the Hurwitz zeta function is defined by

$$\zeta(\alpha, s_{min}, s_{max}) = \zeta(\alpha, s_{min}) - \zeta(\alpha, s_{max}) \ , \tag{23}$$

where

$$\zeta(\alpha, s) = \sum_{i=1}^{\infty} \frac{1}{(i+s)^{\alpha}} \ . \tag{24}$$

We applied the maximum likelihood test to the complementary cumulative distribution for the E values shown in 3 in L=99. For $E = 1.10$, $E = 1.20$ and $E = 13.0$ we obtained slopes with values $\hat{\alpha} = 1.46$, $\hat{\alpha} = 1.34$ and $\hat{\alpha} = 1.50$, respectively. For $E = 1.88$ we divided the distribution in two parts in order to avoid the influence of the bump around avalanches of size 200. For the first part (with $s_{min} = 1$, $s_{max} = 190$) we obtained a slope with value $\hat{\alpha}_1 = 1.69$ and for the second one (considering $s_{min} = 600$, $s_{max} = 1500$) we obtained the value $\hat{\alpha}_2 = 1.57$. All these values are fairly close to the values obtained by the avalanche

distribution collapse.

---

[1] Dante R. Chialvo, Pablo Balenzuela, and Daniel Fraiman, "The brain: What is critical about it?" AIP Conf. Proc. **1028**, 28 (2008).

[2] A. M. Turing, "Computing machines and intelligence," Mind **59**, 433–460 (1950).

[3] D R Chialvo, "Emergent complex neural dynamics," Nat. Phys. **6**, 744–750 (2010).

[4] W L Shew and D Plenz, "The functional benefits of criticality in the cortex," Neuroscientist **19(1)**, 88–100 (2013).

[5] John Beggs, "Editorial: Can there be a physics of the brain?" Phys. Rev. Lett. **114**, 220001 (2015).

[6] P Bak, C Tang, and K Wiesenfeld, "Self-organized criticality: An explanation of 1/f noise," Phys. Rev. Lett. **59(4)**, 381–384 (1987).

[7] O Kinouchi and M Copelli, "Optimal dynamical range of excitable networks at criticality," Nat. Phys. **2**, 348–351 (2006).

[8] L de Arcangelis, C Perrone-Capano, and H J Herrmann, "Self-organized criticality model for brain plasticity," Phys. Rev. Lett. **96**, 028107 (2006).

[9] J M Beggs and N Timme, "Being critical of criticality in the brain," Front. Physiol. **3**, 163 (2012).

[10] Thiago S. Mosqueiro and Leonardo P. Maia, "Optimal channel efficiency in a sensory network," Phys. Rev. E **88**, 012712 (2013).

[11] Malte Henkel, Haye Hinrichsen, and Sven Lübeck, *Non-Equilibrium Phase Transitions* (Springer, Dordrecht, The Netherlands, 2008).

[12] M. N. Barber, "Finite-size scaling," in *Phase Transitions and Critical Phenomena*, Vol. 8, edited by C. Domb and J. L. Lebowitz (Academic Press, New York, USA, 1983).

[13] M E J Newman and G T Barkema, *Monte Carlo Methods in Statistical Physics* (Oxford University Press, New York, UK, 1999).

[14] Annick Lesne and Michel Laguës, *Scale Invariance* (Springer-Verlag, Berlin, Germany, 2012).

[15] Gunnar Pruessner, *Self-Organised Criticality* (Cambridge University Press, Cambridge, UK, 2012).

[16] E. Novikov, A. Novikov, D. Shannahoff-Khalsa, B. Schwartz, and J. Wright, "Scale-similar

activity in the brain," Phys. Rev. E **56(3)**, R2387–R2389 (1997).

[17] Malvin C. Teich, Conor Heneghan, Steven B. Lowen, Tsuyoshi Ozaki, and Ehud Kaplan, "Fractal character of the neural spike train in the visual system of the cat," J. Opt. Soc. Am. A **14**, 529–546 (1997).

[18] K Linkenkaer-Hansen, V V Nikouline, J M Palva, and R J Ilmoniemi, "Long-range temporal correlations and scaling behavior in human brain oscillations," J. Neurosci. **21(4)**, 1370–1377 (2001).

[19] J M Beggs and D Plenz, "Neuronal avalanches in neocortical circuits," J. Neurosci. **23(35)**, 11167–11177 (2003).

[20] J. Andrew Henrie and Robert Shapley, "Lfp power spectra in v1 cortex: The graded effect of stimulus contrast," J. Neurophysiol. **94**, 479–490 (2005).

[21] T L Ribeiro, M Copelli, F Caixeta, H Belchior, D R Chialvo, M A L Nicolelis, and S Ribeiro, "Spike avalanches exhibit universal dynamics across the sleep-wake cycle," PLoS ONE **5(11)**, e14129 (2010).

[22] Gerald Hahn, Thomas Petermann, Martha N. Havenith, Shan Yu, Wolf Singer, Dietmar Plenz, and Danko Nikolić, "Neuronal avalanches in spontaneous activity in vivo," Journal of Neurophysiology **104**, 3312–3322 (2010).

[23] A Haimovici, E Tagliazucchi, P Balenzuela, and D R Chialvo, "Brain organization into resting state networks emerges at criticality on a model of the human connectome," Phys. Rev. Lett. **110**, 178101 (2013).

[24] D. Hermes, K. J. Miller, B. A. Wandell, and J. Winawer, "Stimulus dependence of gamma oscillations in human visual cortex," Cereb. Cortex (2014), 10.1093/cercor/bhu091.

[25] Woodrow L. Shew, Wesley P. Clawson, Jeff Pobst, Yahya Karimipanah, Nathaniel C. Wright, and Ralf Wessel, "Adaptation to sensory input tunes visual cortex to criticality," Nat. Phys. (2015), 10.1038/nphys3370.

[26] Jonathan Touboul and Alain Destexhe, "Power-law statistics and universal scaling in the absence of criticality," arXiv:1503.08033 [q-bio.NC] (2015).

[27] James P. Sethna, Karin A. Dahmen, and Christopher R. Myers, "Crackling noise," Nature **410**, 242–250 (2001).

[28] S. R. Williams and G. J. Stuart, "Dependence of epsp efficacy on synapse location in neocortical pyramidal neurons," Science **295**, 1907–1910 (2002).

[29] Sen Song, Per Jesper Sjöström, Markus Reigl, Sacha Nelson, and Dmitri B Chklovskii, "Highly nonrandom features of synaptic connectivity in local cortical circuits," PLoS Biol. **3(3)**, e68 (2005).

[30] Sandrine Lefort, Christian Tomm, J.-C. Floyd Sarria, and Carl C.H. Petersen, "The excitatory neuronal network of the c2 barrel column in mouse primary somatosensory cortex," Neuron **61(2)**, 301–316 (2009).

[31] A Levina, J M Herrmann, and T Geisel, "Dynamical synapses causing self-organized criticality in neural networks," Nat. Phys. **3**, 857–860 (2007).

[32] Ariadne de Andrade Costa, Mauro Copelli, and Osame Kinouchi, "Can dynamical synapses produce true self-organized criticality?" J. Stat. Mech. , P06004 (2015).

[33] Maurício Girardi-Schappo, Osame Kinouchi, and Marcelo H. R. Tragtenberg, "Critical avalanches and subsampling in map-based neural networks coupled with noisy synapses," Phys. Rev. E **88** (2013), 10.1103/PhysRevE.88.024701.

[34] Rashid V. Williams-García, Mark Moore, John M. Beggs, and Gerardo Ortiz, "Quasicritical brain dynamics on a nonequilibrium widom line," Phys. Rev. E **90**, 062714 (2014).

[35] Janaína K. Andreazza and Leonel T. Pinto, "Simulation of the primary visual cortex of the macaque monkey by natural neural networks," Prooceedings of 2nd LNCC Meeting on Computational Modelling (2006).

[36] J. O'Kusky and M. Colonier, "A laminar analysis of the number of neurons, glia and synapses in the visual cortex (area 17) of adult macaque monkeys," J. Comp. Neurol. **210**, 278–290 (1982).

[37] J. S. Lund, "Spiny stellate neurons," in *The Cerebral Cortex*, Vol. 1, edited by A. Peters and E. G. Jones (Plenum Press, New York, USA, 1984) Chap. 7, pp. 255–308.

[38] E. M. Callaway, "Local circuits in primary visual cortex of the macaque monkey," Annu. Rev. Neurosci. **21(2)**, 47–74 (1998).

[39] N. H. Yabuta and E. M. Callaway, "Functional streams and local connections of layer 4c neurons in primary visual cortex of the macaque monkey," J. Neurosci. **18(22)**, 9489–9499 (1998).

[40] Adam Kohn, "Visual adaptation: Physiology, mechanisms, and functional benefits," J. Neurophysiol. **97(5)**, 3155–3164 (2007).

[41] S. Deutsch and A. Deutsch, *Understanding the Nervous System* (IEEE Press, New York, NY,

USA, 1993).

[42] Silvio C. Ferreira, Claudio Castellano, and Romualdo Pastor-Satorras, "Epidemic thresholds of the susceptible-infected-susceptible model on networks: A comparison of numerical and theoretical results," Phys. Rev. E **86**, 041125 (2012).

[43] Thomas Vojta, "Rare region effects at classical, quantum and nonequilibrium phase transitions," J. Phys. A: Math. Gen. **39**, R143 (2006).

[44] Paolo Moretti and Miguel A. Muñoz, "Griffiths phases and the stretching of criticality in brain networks," Nat. Commun. **4**, 2521 (2013).

[45] William Hoston and A. Nihat Berker, "Multicritical phase diagrams of the Blume-Emery-Griffiths model with repulsive biquadratic coupling," Phys. Rev. Lett. **67**, 1027–1030 (1991).

[46] J.-N. Teramae and Tomoki Fukai, "Local cortical circuit model inferred from power-law distributed neuronal avalanches," J. Comput. Neurosci. **22(3)**, 301–312 (2007).

[47] Robert B. Griffiths, "Nonanalytic behavior above the critical point in a random ising ferromagnet," Phys. Rev. Lett. **23(1)**, 17–19 (1969).

[48] Thomas D. Albright, Thomas M. Jessell, Eric R. Kandel, and Michael I. Posner, "Neural science: A century of progress and the mysteries that remain," Neuron **25**, S1–S55 (2000).

[49] J A Bonachela, S de Franciscis, J J Torres, and M A Muñoz, "Self-organization without conservation: are neuronal avalanches generically critical?" J. Stat. Mech. , P02015 (2010).

[50] Dominic Langlois, Denis Cousineau, and Jean-Philippe Thivierge, "Maximum likelihood estimators for truncated and censored power-law distributions show how neuronal avalanches may be misevaluated," Phys. Rev. E **89**, 012709 (2014).